Design of Serrate-Semi-Circular Riblets with Application to Skin Friction Reduction on Engineering Surfaces

by

Samira Sayad Saravi, Kai Cheng, Tze Pei Chong and Alexandros Vathylakis

Design of Serrate-Semi-Circular Riblets with Application to Skin Friction Reduction on Engineering Surfaces

Samira Sayad Saravi, Kai Cheng, Tze Pei Chong and Alexandros Vathylakis
School of Engineering and Design, Brunel University Cleveland Road,
Uxbridge, UB8 3PH, UK

ABSTRACT

Drag reduction in wall-bounded flows can be achieved by the passive flow control technique through the application of bio-inspired riblet surfaces. This paper presents the innovative design of Serrate-Semi-Circular riblet surfaces particularly focusing on the intrinsic relationship between the riblet features and the turbulent boundary layer structure resulting from these surfaces in engineering applications. The available experimental facilities, instrumentation (i.e. hotwire) and measurement techniques (i.e. velocity spectra) have been employed to investigate the boundary layer velocity profiles and skin friction for flat plate and Serrate-Semi-Circular riblet surfaces. Both the simulation and experimental wind tunnel testing results show that the Serrate-Semi-Circular riblet surface can provide 7% drag reduction, which is better than other riblet configurations, such as V and U shaped ones.

1. INTRODUCTION

In recent years, turbulent boundary layer drag reduction on engineering surfaces has become an important area of fluid dynamics research. Specifically, rising fuel costs have greatly highlighted the usefulness and necessity of developing efficient viscous drag reduction methods. Riblets as a passive method, installed over a smooth surface in the turbulent boundary layer, can reduce drag by approximately 6–8% in turbulent flow. The advantages of using riblets, as a type of micro-structured surfaces in many engineering applications have been recognized as illustrated in Figure 1. For instance, the flight testing of aircrafts with ribleted structural surfaces by Boeing [1], Airbus [2] and NASA [3] demonstrated the important effects of riblets. Sareen [4] also employed different sizes of sawtooth riblets applied to the DU 96-W-180 airfoil for a wind turbine. Apart from the aeronautical applications, other industrial uses for riblets have been identified and in particular, biological surfaces with geometrically complex micro-featured surfaces [5]. In fact, there is now a comprehensive literature regarding effects of riblets with different geometries (Jimenez [6], Choi [7], Bushnell [8], Vukoslavcevic et al. [9], Park and Wallace [10], Lee and Jang [11], Lee and Lee [12], and Bechert et al [13]).

The initial drag reduction studies with riblets include those by Walsh and Weinstein [14] and Walsh [15], [16] at NASA Langley. They used a direct drag balance in a wind tunnel to examine the drag reduction behaviour of various riblet configurations and shapes with sizes of approximately s^+, $h^+ = 10$–15. They were able to reach a drag reduction of up to 4–5% for V, U and L groove riblets, which appeared to be the most effective shapes due to the sharper peaks.

Moreover, the results demonstrated that the aspect ratio h/s of the riblets appears to have a major effect on the drag reduction. However, García-Mayoral and Jiménez [17] suggested that the existing experiments for the location of the breakdown would collapse better with a new length scale, based on the groove area (A_g) rather than with the riblet spacing or depth. They claimed that the degradation for large riblets of the linear regime of drag reduction is not connected with the breakdown of the Stokes behaviour of the longitudinal velocity along the riblet grooves. However, almost all the above research was based on an individual case study basis and very much driven by numerical analysis. It is fundamentally essential to have a scientific understanding of the effects resulting from micro-structured
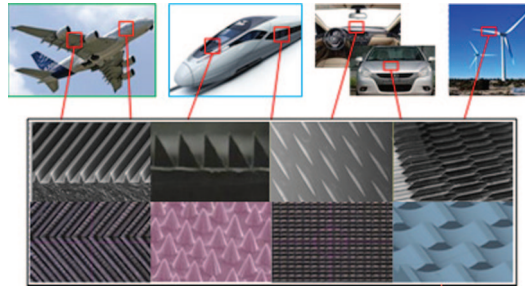
Figure 1. Typical micro-structured surfaces and their engineering applications.
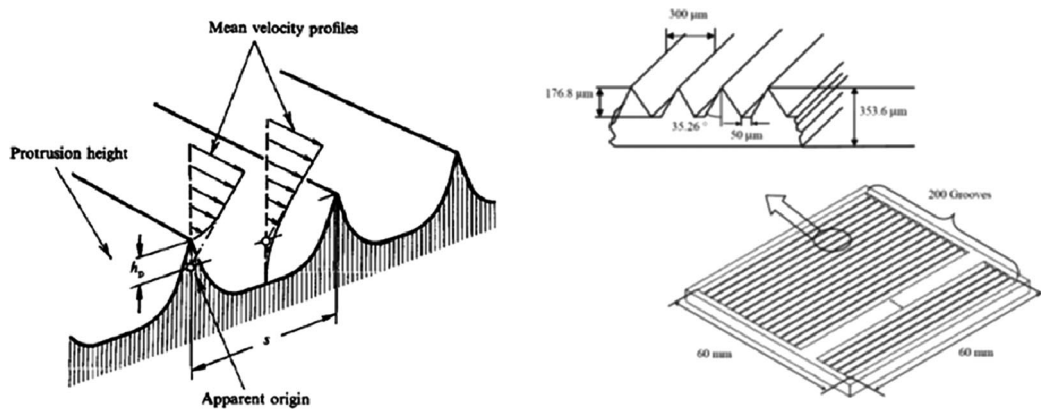

Figure 2. (a) Apparent origin of a U-shape riblet surface (Bechert and Bartnwerfer [18])
(b) Schematic diagram of a V-shape riblet film (Lee and Jang [11]).

surfaces and the associated engineering design principles in order to be able to generate improved and predictive capabilities, especially for drag reduction.

In this paper, the design of innovative Serrate-Semi-Circular riblet surfaces is presented along with the outcomes of the research on transverse modifications of the associated fluid dynamic flow accomplished by the geometrical features of the riblet surface. The Serrate-Semi-Circular Riblet surfaces are designed to delay drag reduction breakdown and to improve the skin friction reduction. Experimental testing on the riblet surfaces was carried out in a wind tunnel aimed at further evaluating and validating the riblet surface design, with the key focus being on examining the velocity profile and skin friction coefficient resulting from the surface design.

2. DESIGN OF SERRATE-SEMI-CIRCULAR RIBLET SURFACE

We have reviewed the regimes for drag reduction in ribleted surfaces, with particular emphasis on the most effective shapes, and the conditions under which that reduction increases [14, 15, 16]. The results lead to the proposal of an alternative shape (Serrate-Semi-Circular riblets), which is analysed to assess its impact on the skin friction. The sizes have been carefully chosen based on the information from the literature review and modelling. Special attention has been given to the effect of serration as wall roughness and the cross sectional area (A_g) [17]. In addition, the effect of having an extra tip inside the riblets on the vortices ejection has been incorporated the design and the size of serration is considered to be in the range of the vortices ones.

The plates employed in the current investigation are made of the aluminium 6082 and the roughness has been measured using the TESA/ZYGO 3D surface profiler, as shown in Figure 4. The dimensions of both plates (riblet and flat plate) are 295 mm × 150 mm × 5 mm and the new design of the riblets has been milled on the flat plate using the fly cutting method.

In order to compare the selected geometry with the literature (Table 6), dimensionless sizes are required, which have been produced by skin friction velocity (u_τ) and kinematic viscosity (v) from experimental data (Table 1). Finally, the base flow velocity was chosen as 30 m/s in this study.
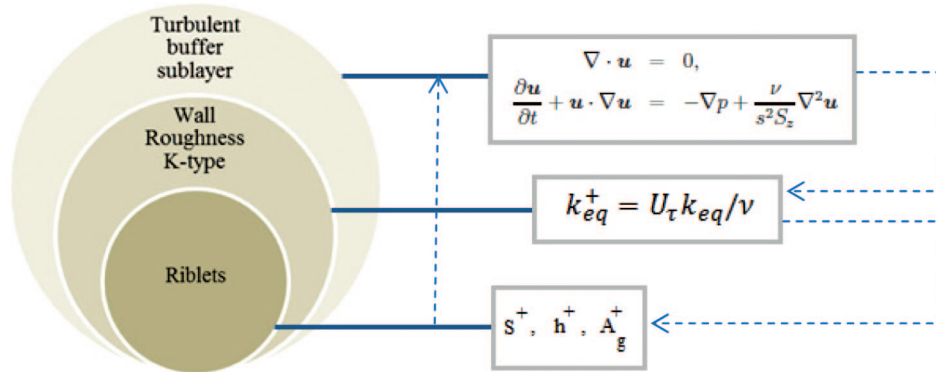
Figure 3. Riblets representing the transitional roughness and the consequent transitional sub-layer of turbulent flow.
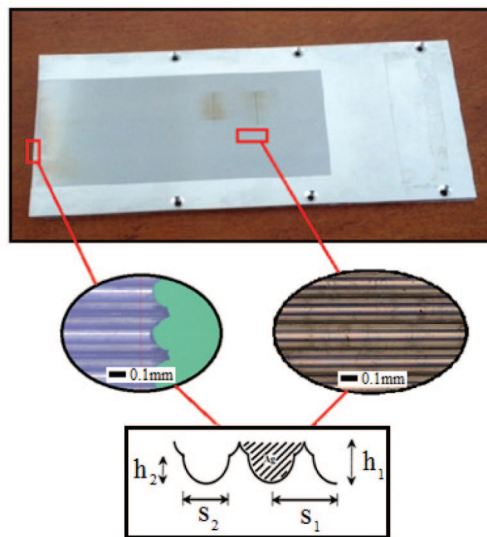

Figure 4. Serrate-Semi-Circular riblets in trailing edge and the middle of test section.

Table 1. The dimensionless and actual (mm) sizes of the designed riblet

Sizes	$h_1^+(h_1)$	$h_2^+(h_2)$	$s_1^+(s_1)$	$s_2^+(s_2)$	$(A_g^+)^{1/2}$
SSC Riblets	10.5 (0.108)	7.5 (0.075)	19.5 (0.210)	14 (0.150)	11

3. EXPERIMENTAL TESTING

This study pertains to the measurement technique for deriving the skin friction and boundary layer structures, inside a wind tunnel over smooth and ribleted surfaces. Recently derived measurements of good quality, using pitot tubes, 5 micron single hot-wire and automated traverse, were used to assess critically, and then to improve the experimental accuracy of, the empirical coefficient as well as the determination of the surface shear and skin friction. Each sensor was calibrated in free-stream flow before and after each profile or each set of data points was measured. If these two calibrations were in disagreement by more than 2–3%, or if the error was more than 0.01, the entire process was repeated.

The experiment was conducted on the vertical blower wind tunnel at Brunel University, as shown in Figure 5 and the dimensions of the test section were 150 mm × 50 mm. This tunnel also had a filter at inlet to remove dust and dirt particles in order to minimize hot-wire contamination and breakage. In addition, sandpaper was used to trigger artificially the boundary layer into being turbulent, which occurred on the plates at zero angle of incidence. This is often referred to as a canonical zero-pressure turbulent gradient boundary layer.
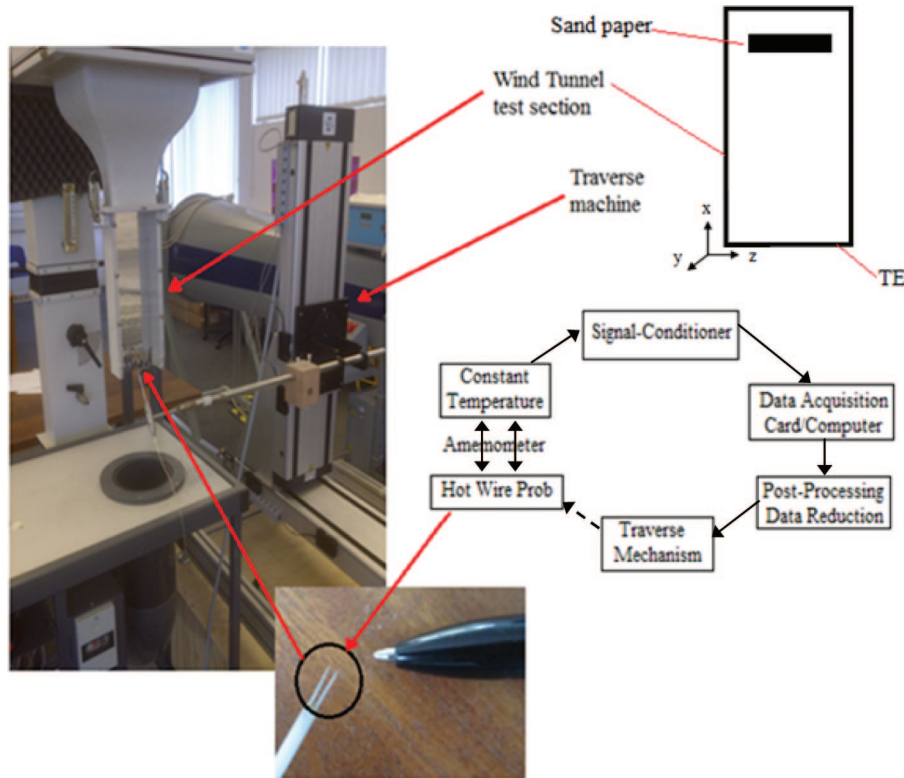
Figure 5. Experimental testing setup by using wind tunnel and hot-wires
data logging system.

The measurements were taken using an automated traverse in the vertical (y), streamwise (x) and spanwise (z) directions, with a displacement accuracy of 0.01mm, 0.01mm and 0.1mm respectively. The traversing machine allows 3-D placement of measurement probes, which can position a thermal probe or pitot tube at any (x, y, z) position and is controlled by the stepper motor, which uses the Thermalpro software on the computer.

The signals from the single hot wire were acquired at 20 kHz, after passing through a 10 kHz anti-aliasing filter and the digitized voltage from the hot wire was then converted to velocity by interpolating the 4th-order polynomial velocity-voltage calibration curve. Voltages were acquired using a National Instruments Data Acquisition DaqBoard/3005 card, which consisted of a 1-MHz A/D with 16-bit resolution, as highlighted in Figure 5.

The collected data from the acquisition card in the first step was reduced by Thermalpro. Next, the mean and root mean square (rms) of the velocity data for the velocity profiles were calculated as:

$$U_{mean} = \frac{1}{N} \Sigma_{i=1}^{N} U_i \tag{1}$$

$$u_{rms} = \sqrt{\frac{1}{N} \Sigma_{i=1}^{N} \left(U_i - U_{mean} \right)^2} \tag{2}$$

where N is the total number of samples in the velocity time series and the rms is a measure of the amount of deviation of a signal piece of data from its mean value, which is computed as the square root of the variance.

Precision uncertainty estimates for the velocity measurements were made through repeatability tests. This is, four replicate velocity profiles were taken for both the smooth and the ribleted surfaces. The systematic error, which represents the bias uncertainty, was obtained from the instrumentation used in the measurements and this was combined with the precision uncertainty to calculate the overall uncertainties for the measured quantities. The method used in this context was that presented by Kline and McClintock [19], which involves examining the derivative of the equation that relates an unknown

Table 2. Uncertainties associated with various measuring devices

Parameter	Device	Typical value	Random error	Uncertainty $(\partial X/X)$ %
Pressure	Microphone	Up to $\approx$250 Pa	$\pm$ 1.25 Pa	$\pm$ 0.50
Ambient Pressure	Barometer	101300 Pa	$\pm$ 10 Pa	$\pm$ 0.01
Temperature	Thermometer	300 K	$\pm$ 1	$\pm$ 0.33
Coordinate(x, y, z)	Traverse	30, 30, 6 (mm)	$\pm$ 0.01, $\pm$ 0.01, $\pm$ 0.1 (mm)	$\pm$ 0.03, $\pm$ 0.03, $\pm$ 1.6

Table 3. Uncertainties associated with derived quantities

Parameter	Typical value	∂Z	Uncertainty %
Density (kg/m^3)	1.2	$\pm$ 0.004	$\pm$ 0.33
Inlet velocity (m/s)	30	$\pm$ 0.1	$\pm$ 0.33

quantity (Z) to measured variables (X,Y). The maximum uncertainty can then be calculated by adding the appropriate uncertainty terms, e.g.:

$$Z = f(X, Y) \tag{3}$$

$$\partial Z = \left[\left(\frac{\partial f}{\partial X} \middle| \partial X \right)^2 + \left(\frac{\partial f}{\partial Y} \middle| \partial Y \right)^2 \right]^{1/2} \tag{4}$$

where ∂X, ∂Y and ∂Z are the uncertainties associated with X, Y and Z, respectively. In order to calculate this equation, ∂X, ∂Y and ∂Z must be known a priori from previous evaluations, instrument specifications or experience. In Tables 2 and 3, uncertainties related to various instruments employed during this investigation are summarised (Sagrado [20]).

4. MODIFICATION OF TBL CHARACTERISTICS

The determination of the onset of transition was achived by careful analysis of the temporal signals of velocity (single hot-wire). This is, the freestream velocity at the inlet of the test section was measured at a distance of 22 mm from the leading edge (U_∞) whilst at the outlet this velocity was measured at the edge of the plate. In addition, because of the effect of the side walls growing towards the leading edge, the inlet velocity was found to be 1.9 % lower than that of outlet. Therefore, the free stream velocity measured at the middle of test section was used to normalise the data.

Figures 6 and 7 show the mean velocity profiles for the flat plate and riblet models. Regarding the riblet case in the present investigation, the velocity profiles shifted slightly downwards when compared
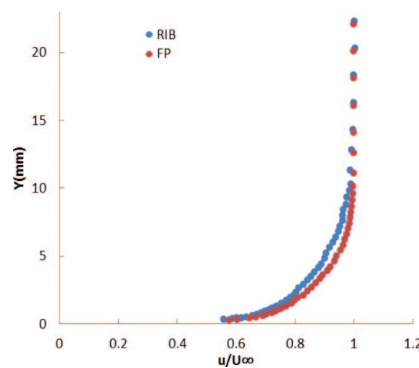

Figure 6. Boundary layer mean velocity profiles at x = 48 (mm) (distance from trailing edge in streamwise direction) positions in the mid spanwise over the riblets and flat plate for Re = 1.42 × 10^5.
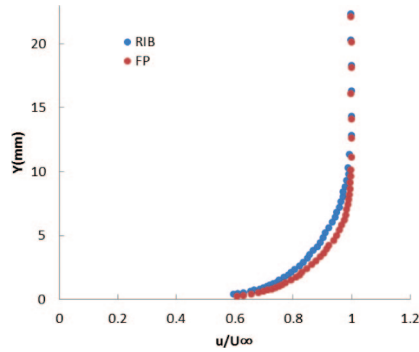
Figure 7. Boundary layer mean velocity profiles at x = 60 (mm) (distance from trailing
edge in streamwise direction) positions in the mid spanwise over the riblets and flat
plate for Re = 1.42×10^5.

with the smooth surface. The fact that friction velocity decreases when using riblets, affects the wall
normal mean velocity gradient which is lower for cases of drag reduction.

In Table 4, the skin friction coefficient (C_f) and freestream velocities of the test section are given for
a smooth surface. The method used to calculate C_f described in the next section. The skin friction
coefficient $C_f = 2\tau_w /\rho U_e^2$ increases with APG, which can be seen in Figure 9, where C_f is presented
for the five different positions of streamwise direction, and this increase is due to the decrease in the
wall shear stress (τ_w).

The obtained results in Table 5 show the effect of riblets on decreasing skin friction and
consequently drag. It can be seen that the skin friction on the ribleted plate has been reduced by 7% in
average when compared to the flat one.

The drag reduction sizes for different studies are presented in Table 6 and the results for research
can be as being favorable when compared to the extant literature. In terms of comparison with V and
U shape riblet geometries, the experiments by Walsh [16] reported a drag reduction of 4% for $s^+ \approx 20$,
and for the DNS by Choi [21] this was around 6% for $s^+ \approx 20$.

Table 4. Free stream velocity and skin friction in the model with
the smooth surface, considered in middle of the test section

Position (z) (mm to mid span)	U∞	C_f
−3.00	26.1347	0.0045–0.0046
−2.00	26.6467	0.0044–0.0045
−1.00	27.3029	0.0044
0	27.0170	0.0044
1.00	27.0662	0.0044–0.0045
2.00	27.0854	0.0045–0.0046
3.00	27.0799	0.0045–0.0046

Table 5. Free stream velocity and skin friction in the model with
the ribleted surface, considered in middle of the test section

Position (z) (mm to mid span)	U∞	C_f
−3.00	26.2971	0.0042
−2.00	26.6081	0.0041–0.0042
−1.00	27.4629	0.0041–0.0042
0	26.9972	0.0041–0.0042
1.00	27.7011	0.0042–0.0043
2.00	28.0609	0.0042
3.00	27.7043	0.0042

Table 6. Optimized riblet's sizes founded in literature; S: simulation,
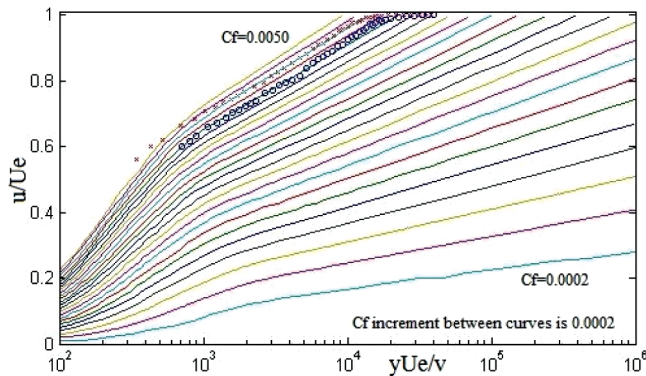E: experiment. (DR: Drag Reduction)

Study	Riblet shapes	s^+	h^+	Modelling Method	DR
Choi (1992) [21]	V	20	17.3	S (DNS)	6%
Walsh (1982) [16]	V	12	12	E	4%
Crawford (1996) [22]	V	20.14	17.70	S (DNS)	5%
Walsh (1982) [16]	U	16	8	E	4%
Park & Wallace (1994) [10]	V	28	14	E	4%
Present study	℧	19	11	E	≈7%

5. SKIN FRICTION COEFFICIENT

The value of the skin friction coefficient C_f was determined by following a method similar to that of Clauser [23]. For a given Mach number, Allen and Tudor [24] proposed a chart with a family of curves of u/U_e versus $(yU_e)/v$ with C_f as the varying parameter. Using a single hot wire allows for measurements inside the Buffer layer ($5 < y^+$ for the size of the riblet is in the range of the buffer layer, the Clauser chart can define local skin friction on both ribleted and smooth surfaces. By plotting the experimental profile on the chart, the skin friction coefficient can be obtained by interpolating between the C_f curves. In Figure 8, the experimental profiles at different positions along the flat plate and riblets are shown. In Figure 9, the experimental profiles at different positions in the middle of the test section along the riblets plate and flat plate are shown. Finally, owing to experimental errors there are fluctuations these riblet results.
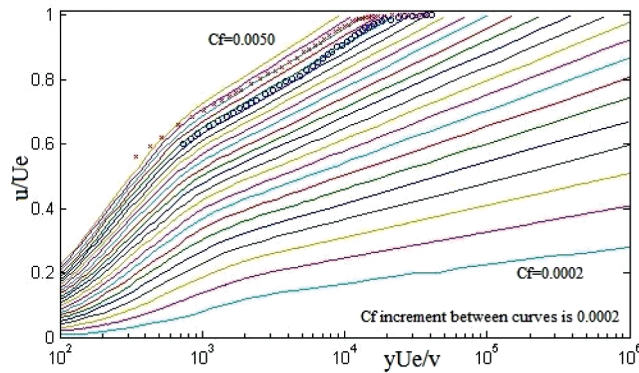
(a)

(b)

Figure 8. Charts used for the determination of the skin friction coefficient C_f from the experimental profiles at different positions over the flat plate (x) and riblets (○) middle of test section: (a) Z = −1(Maximum reduction: 10.86%) (b) Z = 1.
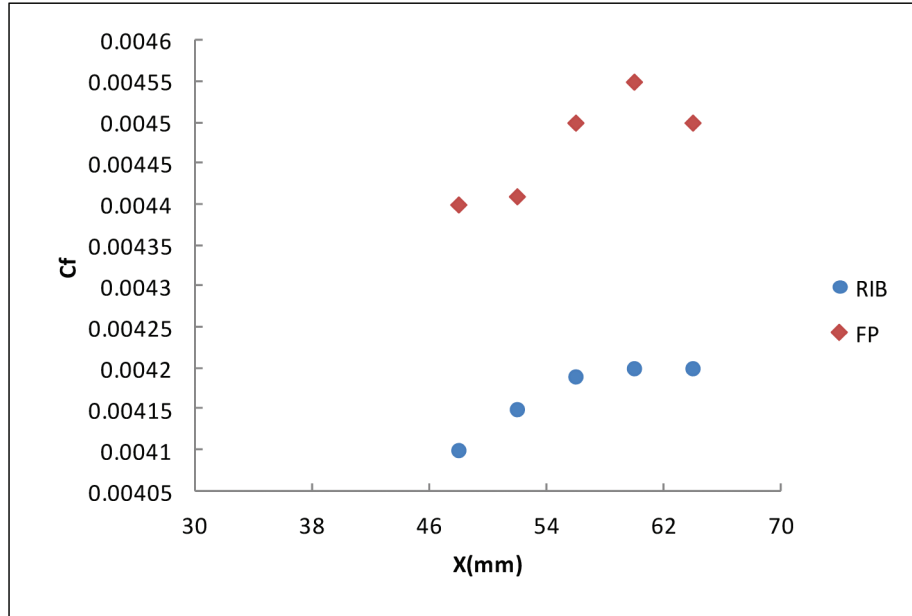
Figure 9. Charts used for the determination of the skin friction coefficient C_f
from the experimental profiles at different streamwise positions
over the flat plate (♦) and riblets (●).

6. CONCLUSIONS

A large portion of the total drag on long objects with relatively flat sides comes from turbulence at the wall, so riblets will have an appreciable effect. Close to the wall itself, the effects of structured surface on the velocity field depend on the specific geometry of the riblets. The selected design dimensions of the Serrate-Semi-Circular riblets are: $s_1^+ = 19.5$, $s_2^+ = 14$, $h_1^+ = 10.5$, $h_2^+ = 7.5$ and $(A_g^+)^{1/2} = 11$. The experimental trials using a vertical wind tunnel were performed on the riblet surface in order to obtain a detailed characterization of the flow parameters and boundary layer profiles under turbulent boundary layers. The skin friction on the riblet plate was reduced by 7% compared to a flat one. In addition, after considering similar riblet spacing (≈ 20) from other researchers, it has emerged that the drag using the riblet structure in the present study decreased by more. Therefore, it can be concluded that this innovative design demonstrates that the groove cross section A_g^+ is a better characterization of drag reduction breakdown than the riblet spacing S^+. However, further investigation is needed to understand the mechanism of the Serrate-Semi-Circular riblets on drag reduction.

ACKNOWLEDGEMENTS

NOTATION

APG	Adverse Pressure Gradient
A_g	Riblets cross section [mm^2]
A_g^+	Dimensionless riblets spacing: $A_g^+ = A_g u_\tau/\nu$, u_τ is friction velocity
C_f	Coefficient of friction: $C_f = \tau_w/(0.5\rho U^2_{ref})$
DR	Drag Reduction
h^+	Dimensionless riblets height: $h^+ = h u_\tau/\nu$, u_τ is friction velocity
h, h_1, h_2	Riblets height [mm]
P	Pressure [Pa]
s^+	Dimensionless riblets spacing: $s^+ = s u_\tau/\nu$, u_τ is friction velocity
s, s_1, s_2	Riblets spacing [mm]
TBL	Turbulent Boundary Layer

TE	Trailing Edge
u	Velocity in the streamwise direction [m/s]
U_∞	Free stream velocity [m/s]
U_e	Velocity at the edge of boundary layer [m/s]
τ_w	Wall shear stress [pa]
u_τ	Skin friction velocity: $u_\tau = (\tau_w/\rho)^{\wedge}(1/2)$[m/s]
V	Velocity in the wall-normal direction [m/s]
ν	Kinematic viscosity [m^2/s]

REFERENCES

[1] McLean JD, Georg-Falvy DN and Sullivan P. Flight test of turbulent skin friction reduction by riblets. In: Conference on Turbulent Drag Reduction by Passive Means, The Royal Aeronautical Society, London, 15–17 September 1987, pp. 408–48.

[2] Coustols E and Savill AM. Turbulent skin-friction drag reduction by active and passive means. AGARD, Report 786 part 1, Seine, France, 1992, pp. 8.1–8.53.

[3] Walsh MJ, Sellers WL and McGinley CB. Riblets drag at flight conditions. J Aircraft 1989; 26(6): 570–575.

[4] Sareen A. Drag reduction using riblet film applied to airfoil for wind turbines. PhD Thesis, University of Illinois at Urbana-Champaign, USA, 2012.

[5] Itoh M, Tamano S, Iguchi R, Yokota K, Akino N, Hino R and Kubo S. Turbulent drag reduction by the seal fur surface. Phys. Fluids 2006; 18 (6): 065102.

[6] Jimenez J, Uhlman M, Pinelli A and Kawahara G. Turbulent shear flow over active and passive porous surfaces. J. Fluid Mech. 2001; 442: 89–117.

[7] Choi KS. European drag-reduction research – Recent developments and current status. Fluid Dynamics Research 1999; 26: 325–335.

[8] Bushnell DM. Aircraft drag reduction – A review. Proc Instn Mech Engrs 2003; 217 (G1): 1–18.

[9] Vukoslavcevic P, Wallace JM and Balint JL. Viscous drag reduction using streamwise aligned riblets. AIAA J 1992; 30: 1119–1122.

[10] Park SR and Wallace JM. Flow alteration and drag reduction by riblets in a turbulent boundary layer. AIAA J 1994; 32 (1): 31–38.

[11] Lee SJ and Jang YG. Control of flow around a NACA 0012 airfoil with a micro-riblet film. J. Fluids Struct. 2005; 20: 659–672.

[12] Lee SJ and Lee SH. Flow field analysis of a turbulent boundary layer over a riblet surface. Exp Fluids 2001; 30: 153–166.

[13] Bechert DW, Bruse M and Hage W. Experiments on drag-reducing surfaces and their optimisation with an adjustable geometry. J. Fluid Mech. 1997; 338: 59–87;

[14] Walsh MJ and Weinstein LM. Drag and heat transfer on surfaces with small longitudinal fins. AIAA J 1978; paper no. 78–1161, New York.

[15] Walsh MJ. Drag characteristics of V-groove and transverse curvature riblets. In: viscous flow drag reduction, progress in Astronautics and Aeronautics, Hough, G.R. (ed.) 1980; 72: 168–184.

[16] Walsh MJ. Turbulent boundary layer drag reduction using riblets, AIAA J 1982; paper no 82–0169, New York.

[17] García-Mayoral R, and Jiménez J. Drag reduction by riblets. Philos. Trans. R. Soc. London, Ser. A 2011; 369: 1412–1427.

[18] Bechert DW and Bartenwerfer M. The viscous flow on surfaces with longitudinal ribs. Journal of Fluid Mechanics. 1989; 206: 105–129.

[19] Kline SJ and McClintock FA. Describing the uncertainties in single sample experiments. Mechanical Engineering. 1953; 3–8.

[20] Sagrado AG. Boundary layer and trailing edge noise sources. PhD Thesis, University of Cambridge, UK, 2007.

[21] Choi H. Turbulent drag reduction: Studies of feedback control and flow over riblets. PhD thesis. Stanford Univ., USA, 1992.

[22] Crawford CH. Direct numerical simulation of near-wall turbulence: passive and active control. PhD thesis. Princeton Univ., New Jersey, USA, 1996.

[23] Clauser FH. Turbulent Boundary Layers in Adverse Pressure Gradient. J. Aeronaut. Sci. 1954; 21: 91–108.

[24] Allen JM, and Tudor DH. Charts for Interpolation of Local Skin Friction from Experimental Turbulent Velocity Profiles. Technical report, Tech. Rep. NASA SP-3048, 1969.